AD___________________

Award Number: W81XWH-04-1-0330

TITLE: Optical Spectroscopy and Multiphoton Imaging for the Diagnosis and Characterization of Hyperplasias in the Mouse Mammary

PRINCIPAL INVESTIGATOR: Melissa Caroline Skala

CONTRACTING ORGANIZATION: Duke University
Durham, NC 27708

REPORT DATE: September 2006

TYPE OF REPORT: Annual Summary

PREPARED FOR: U.S. Army Medical Research and Materiel Command
Fort Detrick, Maryland 21702-5012

DISTRIBUTION STATEMENT: Approved for Public Release;
Distribution Unlimited

REPORT DOCUMENTATION PAGE

Form Approved
OMB No. 0704-0188

1. REPORT DATE *(DD-MM-YYYY)*
01-09-2006

2. REPORT TYPE
Annual Summary

3. DATES COVERED *(From - To)*
1 SEP 2005 - 30 AUG 2006

4. TITLE AND SUBTITLE
Optical Spectroscopy and Multiphoton Imaging for the Diagnosis and Characterization of Hyperplasias in the Mouse Mammary

5a. CONTRACT NUMBER

5b. GRANT NUMBER
W81XWH-04-1-0330

5c. PROGRAM ELEMENT NUMBER

6. AUTHOR(S)
Melissa Caroline Skala

E-Mail: melissa.skala@duke.edu

5d. PROJECT NUMBER

5e. TASK NUMBER

5f. WORK UNIT NUMBER

7. PERFORMING ORGANIZATION NAME(S) AND ADDRESS(ES)

Duke University
Durham, NC 27708

8. PERFORMING ORGANIZATION REPORT NUMBER

9. SPONSORING / MONITORING AGENCY NAME(S) AND ADDRESS(ES)
U.S. Army Medical Research and Materiel Command
Fort Detrick, Maryland 21702-5012

10. SPONSOR/MONITOR'S ACRONYM(S)

11. SPONSOR/MONITOR'S REPORT NUMBER(S)

12. DISTRIBUTION / AVAILABILITY STATEMENT
Approved for Public Release; Distribution Unlimited

13. SUPPLEMENTARY NOTES

14. ABSTRACT: The purpose of the first part of this project is to develop a method to diagnose mammary gland hyperplasias in an animal model in vivo using optical spectroscopy, so that the progression of benign lesions could be studied over time. The absorption and scattering parameters extracted from diffuse reflectance spectra measured in vivo were used to differentiate normal tissue (n=23) and benign lesions (n=16) in the mammary glands of ENU-treated FVBxB6 ApcMin/+ mice. Wilcoxon rank sum tests revealed a statistically significant increase ($p<0.05$) in total hemoglobin concentration for benign lesions compared to the normal mammary gland. Statistically significant differences ($p<0.05$) in the mean reduced scattering coefficient were also found between two sub-classes of benign lesions. The purpose of the second part of this project is to establish fluorescence lifetime imaging of NADH as an in vivo metabolic imaging technique, which could be used for pre-cancer diagnosis and for monitoring cancer therapies. Multiphoton microscopy of the fluorescence lifetime of normal (n=9) and pre-cancerous (n=12) epithelial tissues in vivo revealed a decrease in the lifetime of protein-bound NADH with pre-cancer development ($p<0.05$), and cell culture experiments on MCF10A human breast cells reveal that NADH fluorescence lifetimes are sensitive to changes in oxidative phosphorylation and glycolysis.

15. SUBJECT TERMS
diagnosis, fluorescence, hyperplasia, mouse, multiphoton microscopy, spectroscopy, statistical algorithm

16. SECURITY CLASSIFICATION OF:			**17. LIMITATION OF ABSTRACT**	**18. NUMBER OF PAGES**	**19a. NAME OF RESPONSIBLE PERSON** USAMRMC
a. REPORT U	**b. ABSTRACT** U	**c. THIS PAGE** U	UU	53	**19b. TELEPHONE NUMBER** *(include area code)*

Standard Form 298 (Rev. 8-98)
Prescribed by ANSI Std. Z39.18

Table of Contents

Introduction

The purpose of Tasks 1-2 was to develop a method to diagnose mammary gland hyperplasias in an animal model *in vivo* using optical spectroscopy. The outcomes of this project could lead to the design of an optically based system for *in vivo* diagnosis of mammary gland tumors and hyperplasias, thus allowing research of the hyperplasia-tumor sequence in an animal model. The specific objectives were to measure the optical spectra of tumors, hyperplasias and normal tissues in the mouse mammary gland and to quantitatively identify the optical spectral variables that show the greatest contrast between tumors, hyperplasias and normal tissues in the mouse mammary gland. The results of this work are presented below and were summarized in the previous progress report to the USAMRMC (2005). A post-doc in our laboratory, Greg Palmer, will complete Task 3, and the PI is currently working on Task 4, which is a task that has been added to the approved statement of work (see attached revised statement of work).

Tissue metabolism is known to change with neoplasia development, and the metabolic pathways of cancerous cells can alter the effectiveness of cancer therapies (1). Techniques that can characterize changes in tissue metabolism with neoplastic development *in vivo* could be used for the diagnosis of cancer, and for monitoring cancer treatment. A well-established optical method for measuring changes in the oxidation-reduction state of mitochondria is the “redox ratio”, defined as the fluorescence intensity of FAD (flavin adenine dinucleotide, an electron acceptor in the electron transport chain) divided by NADH (an electron donor in the electron transport chain). NADH fluorescence lifetime imaging (FLIM) is another, relatively unexplored, metabolic imaging technique that measures the time-resolved fluorescence decay of NADH. Previous studies have indicated that NADH fluorescence lifetimes are sensitive to metabolic perturbations *in vitro* (2), but the molecular mechanisms responsible for changes in NADH fluorescence lifetimes are still unclear. NADH has a short and long lifetime component depending on whether it is in a free or protein-bound state (3).

The first goal of Task 4 (which has been added to the approved statement of work) is to determine whether NADH fluorescence lifetimes change with cancer development *in vivo* in an animal model of stratified epithelial cancer (the hamster cheek pouch). Both the mouse mammary gland and the hamster cheek pouch are epithelial tissues, but the hamster cheek pouch is a well-organized, stratified epithelial tissue model. NADH fluorescence is spatially localized to the cellular epithelium in the hamster cheek pouch, but the mouse mammary gland is a more complicated, heterogeneous tissue structure. Thus, *in vivo* imaging studies were carried out on the simpler hamster cheek pouch tissue, but these *in vivo* imaging techniques are translatable to breast cancer research on the mouse mammary gland. The second goal of Task 4 is to characterize changes in NADH fluorescence lifetimes with known chemical and genetic (RNA silencing) perturbations to cellular metabolism in human breast cells in culture. Changes in the redox ratio with these perturbations will also be compared to changes in the NADH fluorescence lifetimes to determine if a relationship exists between these metabolic imaging techniques.

Body

Fluorescence and diffuse reflectance spectra have been measured in 17 ethylnitrosourea (ENU) treated mice *in vivo* (Task 1, parts (a) and (b)). Histological analysis of the measured sites in the mammary gland confirm n=23 normal tissue sites, n=16 hyperplastic sites and n=3 carcinomas (Task 1, part (d)). All of the carcinomas were palpable and none of the hyperplastic lesions were palpable. The variability in normal mammary glands was evaluated with measurements from normal regions of these ENU-treated mice (Task 1, part (c)). This work addresses Task 1 in the statement of work.

The malignant tumors were not included in the optical analysis due to the small sample size. The benign lesions were classified as focal alveolar hyperplasias with some squamous metaplasia, based on the histology. The whole mount analysis revealed two sub-classes of benign lesions: FAH (n=7 sites) and SMT (n=9 sites). Figure 1 shows representative (a) whole mount and (b) histology of one normal site, FAH, SMT, and malignant tumor in the mouse mammary gland. The classification of lesions into FAH or SMT was based on the appearance in the whole mount. FAH were generally more diffuse lesions with a clear appearance of alveolar hyperplasia. SMT, although not palpable, resembled the palpable tumors in that they were frequently more clearly defined and appeared more solid than did the lesions classified as FAH. There were also lesions that shared some aspects of both categories and were classified based on which aspects predominated. Sites classified as "normal" had no abnormal lesions within the areas marked by the pathology ink, or close by.

Meaningful physiological parameters, including total hemoglobin concentration, hemoglobin saturation and tissue scattering have been extracted from the measured diffuse reflectance spectra (Fig. 2). Differences in these physiological parameters between histologically confirmed normal and hyperplastic regions of the mammary gland were evaluated with non-parametric Wilcoxon rank sum tests. There was a statistically significant increase ($p<0.05$) in total hemoglobin concentration for hyperplasia compared to the normal mammary gland. Statistically significant differences ($p<0.05$) in the mean reduced scattering coefficient were found between the two gross sub-classes of hyperplasias (FAH vs. SMT). This work addresses Task 2 (a) for the normal vs. hyperplasia comparison, and Task 2 (c). The fiber optic probe used in this study had a single source-detector separation, so it was not necessary to identify an optimal source-detector separation (Task 2 (b)). *The research above was summarized in the progress report accepted by the USAMRMC last year (2005).*

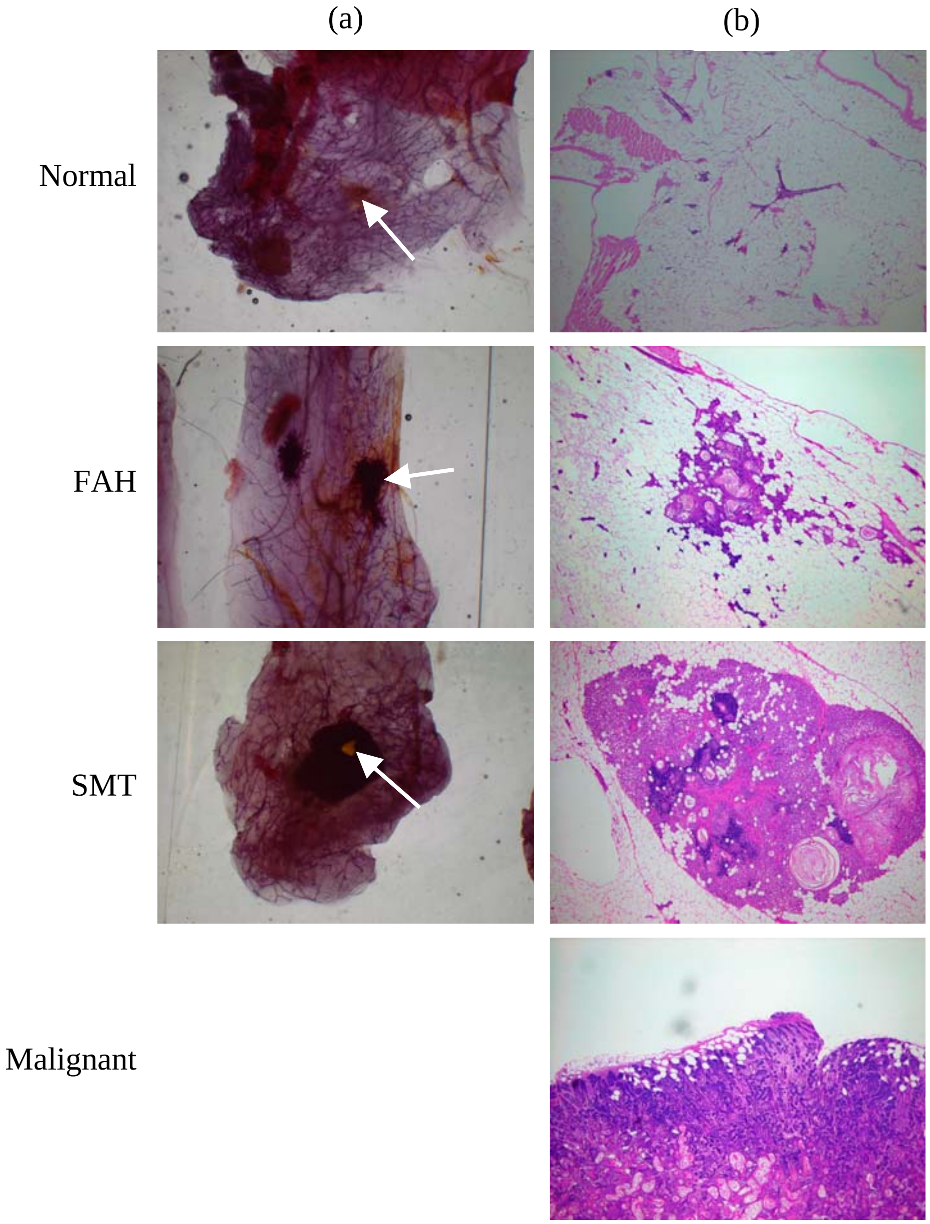

Figure 1: Whole mount images (a) and histology sections (b) from normal, non-malignant (FAH and SMT) and malignant lesions in the mouse mammary gland. FAH and SMT classification was based on gross inspection of the whole mount. All whole mount images are at the same magnification (7x) and all histology images are at the same magnification (40x). Arrows point to measured sites, which were marked with yellow pathology ink.

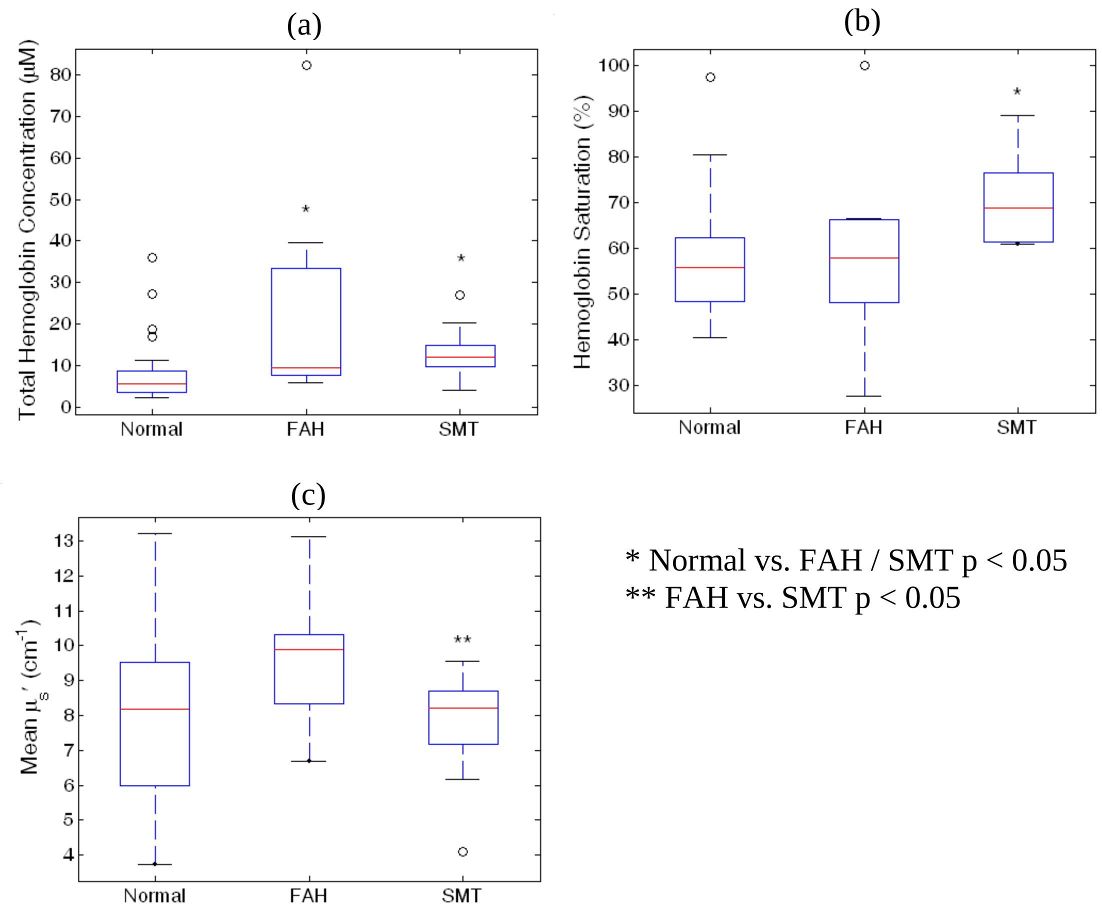

* Normal vs. FAH / SMT $p < 0.05$
** FAH vs. SMT $p < 0.05$

Figure 2: Extracted values for (a) total hemoglobin concentration, (b) hemoglobin saturation and (c) mean reduced scattering coefficient (averaged over the 400-600 nm wavelength range) for normal and non-malignant lesions (FAH and SMT) in the mouse mammary gland. In the boxplots, the box represents the middle 50% of the measurements (the range of the middle 50% of the data is the interquartile range, IQR), the line through the box represents the median of the measurements and the whiskers extend from the box out through all values that are within 1.5 IQRs of the box. Values that are more than 1.5 IQRs away from the box are outliers, and are indicated separately by circles (4). Unpaired Wilcoxon rank sum tests revealed statistically significant differences ($p<0.05$) in the total hemoglobin concentration of normal vs. FAH and normal vs. SMT (Fig. 4 (a)), in the hemoglobin saturation for normal vs. SMT (Fig. 4 (b)), and in mean reduced scattering coefficient for FAH vs. SMT (Fig. 4 (c)). μ_s' = reduced scattering coefficient.

Due to the small sample size, statistical tests were not performed on the carcinomas (n=3). The normal vs. carcinoma comparison for Task 2 (a), and Task 3, which will use electrode measurements of pO_2 to verify tissue oxygenation extracted from measured diffuse reflectance spectra of mouse mammary carcinomas, are currently underway. *A post-doc in our laboratory, Greg Palmer, will complete Task 2 (a) and Task 3, and the PI is currently working on Task 4, which is a task that has been added to the approved statement of work (see attached revised statement of work). The PI asks that Task 3 be removed from the statement of work, and Task 4 be added to the statement of work.*

The following research results (completed work on Task 4) have been submitted for publication to the Journal of Biomedical Optics (see Appendix for submitted manuscript). Multiphoton fluorescence lifetime images (FLIM) of NADH were acquired *in vivo* in 22 hamster cheek pouches, of which 9 were diagnosed as normal (the 9 control animals), 6 were diagnosed with low grade pre-cancer (mild dysplasia and moderate dysplasia) and 6 were diagnosed with high grade pre-cancer (severe dysplasia and CIS). High grade pre-cancers are more likely to progress to cancer than low grade pre-cancers (5). The single SCC sample was not included in the statistical analysis.

The hamster cheek pouch has three distinct layers: an acellular superficial layer, an epithelium and an underlying stroma. Three-dimensional image stacks of fluorescence lifetimes and the fractional contribution of the long lifetime component of these different layers (Figure 3) were used to determine whether multiphoton FLIM can differentiate histologically confirmed normal and dysplastic tissues (Task 4 (a)).

The cytoplasmic fluorescence of the cells in the epithelium of the normal cheek pouch (Fig. 1 (a-c), between 10 - 30 μm depths) has a short (τ_1) and long (τ_2) lifetime component consistent with free and protein-bound NADH, respectively (3, 6) (percent contribution of protein-bound NADH, α_2). The protein-bound NADH lifetime (τ_2) of pre-cancerous and cancerous cells appears to be shorter than normal cells. In the stromal layer of the normal cheek pouch (Fig. 1 (a-c), 40 μm depth) τ_1 is the predominant lifetime component (the contribution of τ_2 is negligible) and its value is similar to the temporal response of the FLIM system and thus is attributed to the second harmonic generation (SHG) of fibrillar collagen (which has a zero lifetime (7)).

Statistical tests also revealed that normal and dysplastic tissues are differentiated with the mean cellular protein-bound NADH lifetime (τ_2) (Table 1). The protein-bound NADH lifetime (τ_2) of both low grade and high grade pre-cancerous cells are statistically lower than normal ($p<0.05$). The relative contribution of protein-bound NADH (α_2) for low grade pre-cancerous cells is also statistically lower than normal (Task 4 (b)). These results demonstrate that multiphoton FLIM of NADH could be a powerful tool for the non-invasive characterization and detection of pre-cancers *in vivo*.

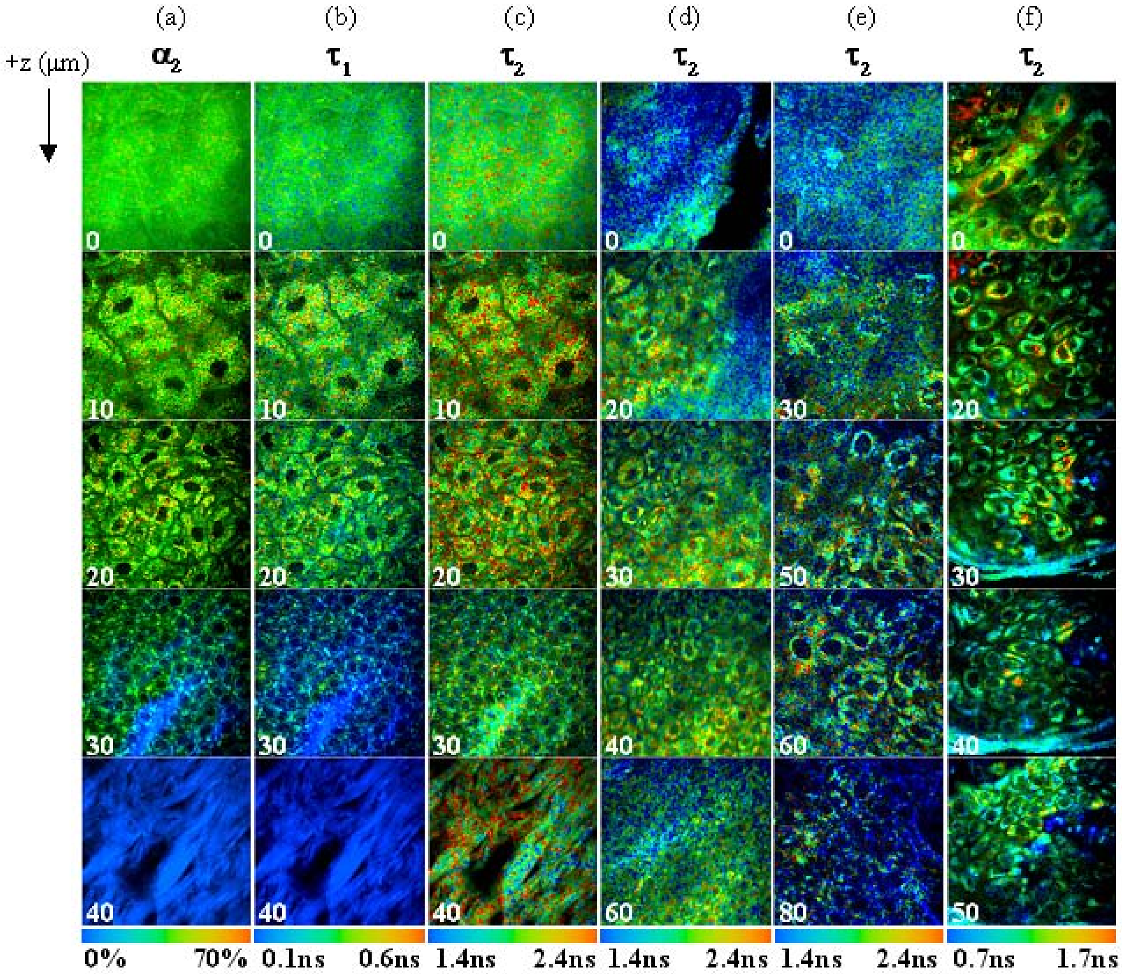

Figure 3: Three-dimensional Multiphoton FLIM images of the normal hamster cheek pouch (a, b, c), low grade pre-cancer (d, mild dysplasia), high grade pre-cancer (e, severe dysplasia), and SCC (f) measured *in vivo* at 780 nm excitation. Images are color coded to values of α_2 (contribution of long lifetime component; a), τ_1 (short lifetime component; b), and τ_2 (long lifetime component; c, d, e, f). The color bar range is at the bottom of each montage. Note that τ_1, τ_2 and α_2 each have a different color scale, and the color scale for (f) is different than (c, d, e). The numbers in the lower left corner of each image indicate the depth below the tissue surface in microns, and each image is 100 μm x 100 μm.

Table 1: NADH fluorescence lifetimes of normal and pre-cancerous cells in the hamster cheek pouch *in vivo*. Mean and standard deviation of cellular τ_2 (protein-bound NADH lifetime) and α_2 (percent contribution of protein-bound NADH) averaged for all cells within an animal for all normal animals (n=9), low grade pre-cancerous animals (n=6) and high grade pre-cancerous animals (n=6) from multiphoton FLIM at 780 nm excitation. Statistically significant differences ($p<0.05$, unpaired Wilcoxon Rank-Sum Tests) exist between normal vs. low grade pre-cancer (*) for τ_2 and α_2, and between normal vs. high grade pre-cancer (*) for τ_2.

	τ_2 (ns)	**α_2 (%)**
Normal (n=9 animals)	2.03 ± 0.06	37 ± 3
Low Grade (n=6 animals)	1.58 ± 0.35*	32 ± 4*
High Grade (n=6 animals)	1.83 ± 0.16*	37 ± 4

* Normal vs. low grade / high grade pre-cancer $p<0.05$

Next, changes in NADH fluorescence lifetimes were characterized with known chemical perturbations to cellular glycolysis and oxidative phosphorylation in MCF10A cell monolayers (Task 4 (c)). Glycolysis was inhibited with 3-bromopyruvate, which inhibits glyceraldehyde-3-phosphate dehydrogenase and 3-phosphoglycerate kinase in a competitive manner (8, 9). Oxidative phosphorylation was inhibited with $CoCl_2$, which mimics hypoxia by increasing the generation of reactive oxygen species during normoxia; up-regulating hypoxia-inducible factor-1α, erythropoietin, and glycolytic enzymes (10, 11).

Multiphoton redox ratio imaging revealed that 3-bromopyruvate produced a statistically significant increase in the redox ratio and $CoCl_2$ produced a statistically significant decrease in the redox ratio in MCF10A monolayers, reflecting an alteration in cellular metabolism with these perturbations (Table 2 (a) and (b)). The results for high density and low density cells are separated because previous work has shown that the cellular lifetime of NADH depends on the cell confluency (due to changes in metabolism with cell confluency) (2). The fluorescence lifetimes at 780 nm excitation ($\tau_1 = 0.30 \pm 0.03$ ns and $\tau_2 = 2.40 \pm 0.07$ ns, averaged for control cells at low and high cell densities) are consistent with free and protein-bound NADH, respectively (3, 6). The fluorescence lifetimes at 890 nm excitation ($\tau_1 = 0.15 \pm 0.01$ ns, $\tau_2 = 2.44 \pm 0.06$ ns, $\alpha_2 = 17 \pm 2$ %, averaged for control cells at low and high cell densities) are consistent with FAD fluorescence (12). Multiphoton FLIM of NADH showed that 3-bromopyruvate caused an increase in the fluorescence lifetime of protein-bound NADH (τ_2) and a decrease in the relative contribution of protein-bound NADH to the overall lifetime decay (α_2) in cells plated at both low and high densities (Table 2 (a) and (b), $p<0.05$). Perturbation with $CoCl_2$ caused a decrease in the fluorescence lifetime of protein-bound NADH (τ_2) and a decrease in α_2 in cells plated at low and high cell densities (Table 2 (a) and (b), $p<0.05$). The results of these characterization studies suggest that protein-bound NADH fluorescence lifetimes could be particularly sensitive to changes in glycolysis and/or oxidative phosphorylation.

Table 2: NADH fluorescence lifetimes and redox ratios of MCF10A cell monolayers. Mean and standard deviation of τ_2 (protein-bound NADH lifetime), α_2 (percent contribution of protein-bound NADH) and the redox ratio [fluorescence intensity of FAD/(NADH+FAD)] for (a) high density control cells (n=8 images from 4 dishes), cells treated with 3-bromopyruvate (n=6 images from 2 dishes), which inhibits glycolysis, and cells treated with $CoCl_2$ (n=6 images from 2 dishes), which inhibits oxidative phosphorylation. Mean and standard deviation of τ_2, and α_2 for (b) low density control cells (n=5 images from 2 dishes), cells treated with 3-bromopyruvate (n=6 images from 2 dishes), and cells treated with $CoCl_2$ (n=6 images from 2 dishes). Statistically significant differences ($p<0.05$, unpaired Wilcoxon Rank-Sum Tests) exist between control vs. 3-bromopyruvate treated and control vs. $CoCl_2$ treated cells for the variables marked with an asterisk (*). The multiphoton FLIM excitation wavelength is 780 nm, and the cells are MCF10A breast epithelial cells.

(a)

High Density	**τ_2 (ns)**	**α_2 (%)**	**FAD/(NADH+FAD)**
Control (n=8 images)	2.37 ±0.02	30 ± 1	0.60 ± 0.03
3-bromopyruvate (n=6 images)	2.42 ± 0.01*	28 ± 1*	0.70 ± 0.05*
$CoCl_2$ (n=6 images)	2.31 ± 0.03*	28 ± 1*	0.52 ± 0.02*

*Control vs. 3-bromopyruvate / $CoCl_2$ $p<0.05$

(b)

Low Density	**τ_2 (ns)**	**α_2 (%)**	**FAD/(NADH+FAD)**
Control (n=5 images)	2.44 ± 0.02	30 ± 1	0.55 ± 0.02
3-bromopyruvate (n=6 images)	2.52 ± 0.02*	28 ± 1*	0.64 ± 0.02*
$CoCl_2$ (n=6 images)	2.38 ± 0.01*	27 ± 1*	0.52 ± 0.01*

*Control vs. 3-bromopyruvate / $CoCl_2$ $p<0.05$

The remaining tasks to be completed include Task 4 (d-f). In these tasks, RNA silencing will be used to inhibit NADH from binding to lactate dehydrogenase (LDH), which is known to be up-regulated in cancers of the breast (14). The fluorescence lifetime of protein-bound NADH has been shown to change depending on the enzyme it is bound to in solution (15), and RNA silencing of LDH will be used to determine if NADH lifetimes are sensitive to inhibition of specific protein binding in the cell environment (MCF7 human breast cancer cell monolayers). The redox ratio will also be measured to determine whether inhibition of LDH-NADH binding produces similar changes in the redox ratio and NADH fluorescence lifetimes. Preliminary work indicates a ~50% decrease in LDH activity for siRNA treated cells compared to a negative control. Future studies will determine whether this decrease in LDH-NADH binding produces measurable changes in the NADH fluorescence lifetime and redox ratio of MCF7 human breast cancer cells.

Key Research Accomplishments

- Measured fluorescence and diffuse reflectance of ethylnitrosourea (ENU) treated mouse mammary glands over the entire ultraviolet to visible (UV-VIS) wavelength range *in vivo*.
- Quantitatively identified the optical spectral variables that show the greatest contrast between hyperplasias and normal regions of the mouse mammary gland.
- Quantitatively identified the optical spectral variables that show the greatest contrast between sub-groups of mammary gland hyperplasias
- Measured the fluorescence lifetime of NADH in 9 normal and 12 pre-cancerous tissues *in vivo*
- Identified changes in the NADH fluorescence lifetime and morphology of normal and pre-cancerous epithelial tissues from the *in vivo* fluorescence lifetime images
- Characterized changes in the fluorescence lifetime and redox ratio with known *chemical* perturbations to cellular metabolism in human breast cells (MCF10A) in culture

Manuscripts in review

- Melissa C. Skala, Kristin M. Riching, Damian K. Bird, Annette Gendron-Fitzpatrick, Jens Eickhoff, Kevin W. Eliceiri, Patricia J. Keely, Nirmala Ramanujam. In vivo Multiphoton Fluorescence Lifetime Imaging of Free and Protein-bound NADH in Normal and Pre-cancerous Epithelia. Journal of Biomedical Optics, 2006, *in review*.

Invited book chapters in press

- Melissa C. Skala, Kevin W. Eliceiri, Nirmala Ramanujam "Multiphoton Laser Scanning Microscopy for Diagnosing Epithelial Precursors and Cancers" in Methods in Cell Biology, *in press*

Reportable Outcomes

Journal articles

- Melissa C. Skala, Jayne M. Squirrell, Kristin M. Vrotsos, Jens C. Eickhoff, Annette Gendron-Fitzpatrick, Kevin W. Eliceiri, Nirmala Ramanujam. Multiphoton microscopy of endogenous fluorescence differentiates normal, pre-cancerous and cancerous squamous epithelial tissues, Cancer Research 65:(4); 1180-1186 (2005).
- Melissa C. Skala, Gregory M. Palmer, Changfang Zhu, Quan Liu, Kristin M. Vrotsos, Crystal L. Marshek-Stone, Annette Gendron-Fitzpatrick, and Nirmala Ramanujam. Investigation of fiber-optic probe designs for optical spectroscopic diagnosis of epithelial pre-cancers. Lasers in Surgery and Medicine 34; 25-38, 2004.

Conference presentations

- Melissa C. Skala, Kristin M. Riching, Annette Gendron-Fitzpatrick, Kevin W. Eliceiri, Nirmala Ramanujam. “In vivo multiphoton microscopy of metabolic oxidation-reduction states and NADH fluorescence lifetimes in normal and pre-cancerous epithelia.” Gordon Research Conference: Lasers in Medicine & Biology, (2006).
- Melissa C. Skala, Kristin M. Riching, Damiain K. Bird, Kristin M. Vrotsos, Annette Gendron-Fitzpatrick, Kevin W. Eliceiri, Nirmala Ramanujam. “In vivo Multiphoton Fluorescence Lifetime Imaging of Free and Protein-Bound NADH in Normal and Pre-Cancerous Epithelia.” Optical Society of America: Biomedical Topical Meeting (2006).
- Melissa C. Skala, Gregory M. Palmer, Benjamin J. Sprague, Ruth Sullivan, Amy R. Moser, Nirmala Ramanujam. “Optical Properties Differentiate Normal, Malignant and Non-Malignant Lesions in the Mouse Mammary Gland.” Era of Hope Meeting (Department of Defense Breast Cancer Research Program) (2005).
- Melissa C. Skala, Damian K. Bird, Kristin M. Riching, Kristin M. Vrotsos, Kevin W. Eliceiri, Annette Gendron-Fitzpatrick, John G. White, Nirmala Ramanujam. “In vivo Multiphoton Fluorescence Lifetime Imaging Microscopy of NADH in Normal and Pre-cancerous Epithelial Tissues.” Engineering Conferences International: Advances in Optics for Biotechnology, Medicine and Surgery (2005).
- Melissa C. Skala, Jayne M. Squirrell, Kristin M. Vrotsos, Annette Gendron-Fitzpatrick, Jens Eickhoff, Kevin W. Eliceiri, Nirmala Ramanujam. “Multiphoton imaging of endogenous fluorescence in neoplastic and non-neoplastic epithelial tissues.” Gordon Research Conference: Lasers in Medicine & Biology, (2004).
- Melissa C. Skala, Jayne M. Squirrell, Kristin M. Vrotsos, Annette Gendron-Fitzpatrick, Kevin W. Eliceiri, Nirmala Ramanujam. “Multiphoton imaging of endogenous fluorescence in neoplastic and non-neoplastic epithelial tissues.” Optical Society of America: Biomedical Topical Meeting (2004).
- Melissa C. Skala, Jayne M. Squirrell, Kristin M. Vrotsos, Kevin W. Eliceiri, Nirmala Ramanujam. “Depth-resolved fluorescence imaging of neoplastic and non-neoplastic epithelial tissues.” Annual Meeting of the American Society for Laser Medicine and Surgery (2004).

Degrees obtained and progress toward PhD:

- Master of Science, Biomedical Engineering, May 2004
- Passed the preliminary exam at Duke University, June 2006

Awards and honors:

- Invited Speaker, “Metabolic Imaging of Neoplasia”, Imperial College, London, 2006
- American Society for Laser Medicine and Surgery competitive summer research grant, 2004
- American Society for Laser Medicine and Surgery national meeting competitive travel grant, 2004

Conclusions

Normal and hyperplastic regions of the mouse mammary gland have been differentiated *in vivo* with optical spectroscopy (Tasks 1-2). Two different sub-classes of hyperplasias have also been differentiated with optical spectroscopy *in vivo*. At present we do not know if these two classes of hyperplasias represent stages of progression from hyperplasia to malignancy, or whether they represent two different types of benign lesions. However, this preliminary study indicates that optical spectroscopy could be used to follow the two classes of hyperplasias in the mammary gland *in vivo* over time to determine whether the lesions remain benign or become malignant, and these time course experiments will allow for a greater understanding of disease progression in animal models of breast cancer. The physical features used to differentiate mouse mammary lesions in this study may offer insight into the biological basis for the difference between normal and non-malignant lesions.

Normal and pre-cancerous epithelial tissues were differentiated with the NADH fluorescence lifetime using multiphoton FLIM of the hamster cheek pouch *in vivo* (Task 4 (a-b)). The techniques developed on the simple tissue structure of the hamster cheek pouch could be translated to more complex animal models of breast cancer progression *in vivo*. Chemical perturbations of breast cancer cells in culture indicate that the redox ratio and NADH fluorescence lifetimes are sensitive to similar changes in glycolysis and oxidative phosphorylation (Task 4 (c)). Future studies on human breast cancer cell monolayers (MCF7) will determine whether inhibition of specific NADH binding sites in the cell environment (using RNA silencing) affect the NADH fluorescence lifetime and redox ratio (Task 4 d-f).

References

1. Gulledge, C. J. & Dewhirst, M. W. (1996) *Anticancer Res* **16,** 741-9.
2. Bird, D. K., Yan, L., Vrotsos, K. M., Eliceiri, K. W., Vaughan, E. M., Keely, P. J., White, J. G. & Ramanujam, N. (2005) *Cancer Res* **65,** 8766-73.
3. Lakowicz, J. R., Szmacinski, H., Nowaczyk, K. & Johnson, M. L. (1992) *Proc Natl Acad Sci U S A* **89,** 1271-5.
4. Gibbons, J. & Chakraborti, S. (1992) *Nonparametric Statistical Inference* (Marcel Dekker, New York).
5. Sawaya, G. F., Brown, A. D., Washington, A. E. & Garber, A. M. (2001) *N Engl J Med* **344,** 1603-7.
6. Schneckenburger, H., Wagner, M., Weber, P., Strauss, W. S. L. & Sailer, R. (2004) *J. Fluorescence* **14,** 649-54.
7. Campagnola, P. J. & Loew, L. M. (2003) *Nat Biotechnol* **21,** 1356-60.
8. Jones, A. R., Gillan, L. & Milmlow, D. (1995) *Contraception* **52,** 317-20.
9. Lee, A. W. & States, D. J. (2006) *Cell Death Differ*.
10. Chandel, N. S., Maltepe, E., Goldwasser, E., Mathieu, C. E., Simon, M. C. & Schumacker, P. T. (1998) *Proc Natl Acad Sci U S A* **95,** 11715-20.
11. Hervouet, E., Pecina, P., Demont, J., Vojtiskova, A., Simonnet, H., Houstek, J. & Godinot, C. (2006) *Biochem Biophys Res Commun* **344,** 1086-93.
12. Tanaka, F., Tamai, N. & Yamazaki, I. (1989) *Biochemistry* **28,** 4259-62.

13. Banerjee, S. & Bhatt, D. K. (1989) *Indian J Cancer* **26,** 21-30.
14. Szutowicz, A., Kwiatkowski, J. & Angielski, S. (1979) *Br J Cancer* **39,** 681-7.
15. Iweibo, I. (1976) *Biochim Biophys Acta* **446,** 192-205.

Appendices

1. Revised Statement of Work

2. Melissa C. Skala, Kristin M. Riching, Damian K. Bird, Annette Gendron-Fitzpatrick, Jens Eickhoff, Kevin W. Eliceiri, Patricia J. Keely, Nirmala Ramanujam. In vivo Multiphoton Fluorescence Lifetime Imaging of Free and Protein-bound NADH in Normal and Pre-cancerous Epithelia. Journal of Biomedical Optics, 2006, *in review*.

STATEMENT OF WORK

Optical Spectroscopy for the Diagnosis and Characterization of Hyperplasias in the Mouse Mammary Gland
Melissa C. Skala, Predoctoral Trainee

Task 1: To measure fluorescence and diffuse reflectance of ethylnitrosourea (ENU) treated mouse mammary glands over the entire ultraviolet to visible (UV-VIS) wavelength range *in vivo* (months 1-7).

a. Measure fluorescence and diffuse reflectance spectra over the UV-VIS wavelength range from tumors, hyperplasias and normal regions of the surgically exposed mammary glands of 5 mice *in vivo* to optimize instrument settings and animal preparation (months 1-3).

COMPLETED

b. Measure fluorescence spectra over the UV-VIS wavelength range from tumors, hyperplasias and normal regions of the surgically exposed mammary glands of ~15 mice *in vivo* (the sample size will be modified based on the outcome of the statistical algorithm) (months 3-7).

COMPLETED

c. Measure fluorescence spectra over the UV-VIS wavelength range from mice not treated with ENU to assess the variability in normal mammary glands between mice and with mouse age. Measurements will be made from the surgically exposed mammary glands of ~10 mice *in vivo* (the sample size will be modified based on the outcome of the statistical algorithm) (months 3-7).

Normal variability determined from measurements of normal sites in ENU-treated mice

d. Histologically evaluate all mammary gland sites from which spectroscopic data has been obtained (months 3-7).

COMPLETED

Task 2: To quantitatively identify the optical spectral variables that show the greatest contrast between tumors, hyperplasias and normal regions of the mouse mammary gland (months 6-20).

a. Use statistical algorithms to determine the accuracy of optical spectroscopy in differentiating tumors, hyperplasias and normal tissue sites in the mouse mammary gland, and identify the optimal excitation-emission wavelengths for discriminating tissue types (months 6-12).

Normal vs. hyperplasia comparison completed, tumor comparison to be completed by Greg Palmer in conjunction with Task 3.

b. Use statistical algorithms to identify the optimal source-detector separation for discriminating tumors, hyperplasias and normal regions of the mouse mammary gland (11-16).

The fiber optic probe used in this study had a single source-detector separation, so this task is no longer necessary.

c. Use statistical algorithms to differentiate potential sub-groups of mammary gland hyperplasias (months 15-20).

COMPLETED

A post-doc in our lab, Greg Palmer, is currently working on *Task 3* and will complete this work. The PI will focus on a *Task 4*, and asks that *Task 4* be added to the Approved Statement of Work, and that *Task 3* be removed from the Approved Statement of Work.

Task 3: Use a physical model to extract optical properties from measured tissue fluorescence and diffuse reflectance spectra in R3230 rodent mammary carcinomas and verify the tissue oxygenation results with electrode measurements of pO_2 (months 18-36)

a. Determine optimal probe geometry for desired penetration depth in normal tissue and tumors (months 18-20).
b. Establish a protocol for *in vivo* spectroscopy and electrode measurements of mammary carcinomas in 5 rats (months 20-24).
c. Measure fluorescence and diffuse reflectance spectra, and pO_2 in 15 mammary glands with tumor(s) and 15 normal mammary glands *in vivo* (months 24-32).
d. Use a physical model to extract tumor and normal mammary gland optical properties, and verify extracted tissue oxygenation with electrode measurements of pO_2 (months 30-36).
e. Histologically evaluate all mammary gland sites from which spectroscopy and electrode data has been obtained (months 30-36).

The PI asks for this task to be added to the Approved Statement of Work

Task 4: Identify the sources of endogenous fluorescence contrast between normal and pre-cancerous tissues in the hamster cheek pouch model of epithelial carcinogenesis, and characterize these changes with controlled experiments on MCF10A and MCF7 human breast cells (months 18-36)

a. Measure the fluorescence lifetime of NADH in 9 normal and 12 pre-cancerous tissues *in vivo* (months 14-18).

COMPLETED

b. Identify changes in the NADH fluorescence lifetime and morphology of normal and pre-cancerous epithelial tissues from the *in vivo* fluorescence lifetime images (months 18-24).

COMPLETED

c. Characterize changes in the fluorescence lifetime and redox ratio with known *chemical* perturbations to cellular metabolism in human breast cells (MCF10A) in culture (months 22-24).

COMPLETED

d. Determine an optimal protocol for altering the metabolism of human breast cells (MCF7) with *genetic* perturbations using RNA silencing (months 24-28).

Currently in progress

e. Measure the optical redox ratio and fluorescence lifetime of genetically perturbed MCF7 cells using confocal microscopy (months 28-34).

To be completed

f. Characterize changes in the fluorescence lifetime and the redox ratio with neoplastic development *in vivo* with known *genetic* perturbations to human breast cells (MCF7) in culture using RNA silencing techniques (months 32-36).

To be completed

Product/Deliverables: Upon completion, each task will be disseminated in the form of one or more conference presentations, as well as in the form of a peer-reviewed journal article.

In vivo Multiphoton Fluorescence Lifetime Imaging of Free and Protein-bound NADH in Normal and Pre-cancerous Epithelia

Melissa C. Skala[1], Kristin M. Riching[2], Damian K. Bird[3,†], Annette Gendron-Fitzpatrick[4], Jens Eickhoff[5], Kevin W. Eliceiri[3], Patricia J. Keely[6], Nirmala Ramanujam[1*]

[1]Department of Biomedical Engineering, Duke University, Durham, NC 27708
[2]Department of Biomedical Engineering, University of Wisconsin, Madison, WI 53706
[3]Laboratory for Optical and Computational Instrumentation, University of Wisconsin, Madison, WI 53706
[4]Research Animal Resources Center, University of Wisconsin, Madison, WI 53706
[5]Department of Biostatistics and Medical Informatics, University of Wisconsin, Madison, WI 53706
[6]Department of Pharmacology, University of Wisconsin, Madison, WI 53706

[†]Current Address: Photophysics and Photochemistry Group, University of Melbourne, Victoria 3010, Australia

*For Correspondence:
Nirmala Ramanujam
Dept. Biomedical Engineering
Duke University
Rm. 2575 CIEMAS
Durham, NC 27708-0281
Phone: 660-5307
Fax:(919) 684-4488
Email: nimmi@duke.edu

Running Title: Fluorescence Lifetime Imaging of Pre-cancer

Key words: metabolism, oral cancer, multiphoton microscopy, animal model

Abbreviations: Fluorescence Lifetime Imaging Microscopy (FLIM), Second Harmonic Generation (SHG), dimethylbenz[α]anthracene (DMBA), Carcinoma in Situ (CIS), Squamous Cell Carcinoma (SCC)

ABSTRACT

Multiphoton fluorescence lifetime imaging microscopy (FLIM) is a three-dimensional functional imaging technique with cellular resolution. This is the first study to investigate the potential for *in vivo* pre-cancer diagnosis with metabolic imaging via multiphoton FLIM of the endogenous metabolic co-factor, NADH. This technique provides information on the metabolic state of tissue without exogenous contrast agents or tissue biopsy. The dimethylbenz[α]anthracene (DMBA)-treated hamster cheek pouch model of oral carcinogenesis was imaged using multiphoton FLIM at 780 nm excitation. The cytoplasm of normal hamster cheek pouch epithelial cells had short (0.29 ± 0.03 ns) and long lifetime components (2.03 ± 0.06 ns), attributed to free and protein-bound NADH, respectively. The underlying structural protein had no measurable lifetime, which reflected a second harmonic generated (SHG) signal from collagen fibrils. Low grade pre-cancers (mild to moderate dysplasia) and high grade pre-cancers (severe dysplasia and carcinoma in situ) were discriminated from normal tissues by their decreased protein-bound NADH lifetime and increased nuclear diameter. Inhibition of cellular glycolysis and oxidative phosphorylation in cell culture produced an increase and decrease, respectively, in the protein-bound NADH lifetime. This indicates that the decrease in protein-bound NADH lifetime with dysplasia is due to a shift from oxidative phosphorylation to glycolysis, consistent with the predictions of neoplastic metabolism. This study demonstrates that multiphoton FLIM is a powerful tool for the non-invasive characterization and detection of epithelial pre-cancers *in vivo*.

Introduction

Fluorescence lifetime imaging microscopy (FLIM) is a functional imaging technique that probes the excited state lifetime of a fluorophore. The excited state lifetime can be altered by the fluorophore microenvironment, including factors such as local pH, temperature, viscosity and oxygen concentration (1). FLIM, which relies on the temporally resolved fluorescence signal, is advantageous over fluorescence intensity or spectral measurements for small volume tissue imaging because it is independent of fluorophore concentration, and minimally affected by tissue absorption and scattering, and fluctuations in excitation intensity (2). Multiphoton excited FLIM can generate three-dimensional images of fluorophore lifetimes with cellular and sub-cellular resolution (1). The near infrared (NIR) excitation used in multiphoton microscopy (3) allows for greater penetration depths (4) and improved tissue viability (5) compared to single-photon excitation. An intuitive application of multiphoton FLIM is to exploit the endogenous fluorescence contrast from electron carriers, reduced nicotinamide adenine dinucleotide (NADH) and flavin adenine dinucleotide (FAD) already present in tissue for the early detection of cancer.

One of the hallmarks of carcinogenesis is a shift from cellular oxidative phosphorylation to cellular glycolysis for ATP production (Warburg Effect (6, 7)). The endogenous fluorophore NADH is the principal electron acceptor in glycolysis and electron donor in oxidative energy metabolism. NADH has a short and long lifetime component, respectively depending on whether it is in a free or protein-bound state (8). The short lifetime of NADH in its free state is due to dynamic quenching by the adenine moiety (2). Many enzymes bind to NADH in the metabolic pathway (9), and as favored metabolic pathways shift with cancer progression, the distribution of NADH binding sites change (10). The fluorescence lifetime of protein-bound NADH changes depending on the enzyme it is bound to (11). This suggests that changes in metabolism with cancer development can be probed by the lifetime of protein-bound NADH.

The goal of our work was to exploit multiphoton FLIM of protein-bound NADH for metabolic imaging of epithelial pre-cancers *in vivo*. To our knowledge, this is the first study to image changes in the lifetime of protein-bound NADH and relative abundance of free and protein-bound NADH with neoplastic progression *in vivo*. The study described in this paper consists of two parts. In the first part of the study, changes in the lifetime of protein-bound NADH and relative abundance of free and protein-bound NADH with inhibition of specific metabolic pathways were quantified. Specifically, multiphoton FLIM was carried out on an MCF10A cell culture model before and after inhibition with 3-bromopyruvate or cobalt chloride ($CoCl_2$). Glycolysis was inhibited with 3-bromopyruvate, which inhibits glyceraldehyde-3-phosphate dehydrogenase and 3-phosphoglycerate kinase in a competitive manner (12, 13). Oxidative phosphorylation was inhibited with $CoCl_2$, which mimics hypoxia by increasing the generation of reactive oxygen species during normoxia; up-regulating hypoxia-inducible factor-1α, erythropoietin, and glycolytic enzymes (14, 15). $CoCl_2$ and 3-bromopyruvate produced a decrease and increase, respectively in the lifetime of protein-bound NADH, and both perturbations produced a decrease in the abundance of protein-bound NADH relative to free NADH. The results of these characterization studies suggest that protein-bound

NADH fluorescence lifetimes would be particularly sensitive to changes in glycolysis and/or oxidative phosphorylation.

In the second part of the study, multiphoton FLIM was used to investigate the lifetime of protein-bound NADH and the relative abundance of free and protein-bound NADH in normal and dysplastic tissues in the dimethylbenz[α]anthracene (DMBA)-treated hamster cheek pouch model of carcinogenesis at 780 nm excitation. The DMBA treated hamster cheek pouch model was selected for this study because it has been shown to mimic the dysplasia-carcinoma sequence in the human oral cavity (16-18) and different stages of dysplasia and carcinoma can be examined over a relatively short period of time. The results of this study indicate that the protein-bound NADH lifetime decreases with low grade pre-cancers (mild to moderate dysplasia) and high grade pre-cancers (severe dysplasia and carcinoma in situ (CIS)) compared to normal tissues, and the abundance of protein-bound NADH relative to free NADH decreases with low grade pre-cancers *in vivo*.

Materials and Methods

Imaging Instrumentation

Two separate custom designed multiphoton time-domain lifetime systems were employed at the University of Wisconsin for the cell culture and *in vivo* experiments. The system used for cell culture experiments was constructed around a Nikon Eclipse TE300 (19). A titanium-sapphire laser (Spectra-Physics-Millennium/Tsunami, 82 MHz, 100 fs) pumped by a 5 W Millenia was used as an excitation source at 780 nm excitation for FLIM, and at both 780 nm and 890 nm excitation for intensity imaging. Other components include a Nikon 40x Plan Apo oil-immersion lens (N.A. =1.3), and a dichromatic mirror (BG39, Schott, Elmsford, NY) that allowed the 780 nm excitation light to reflect onto the sample and wavelengths between 400 nm and 600 nm to transmit to the detector. . Intensity and FLIM data were collected pixel-by-pixel by a laser scanning unit (based on a BioRad, MRC-600) and a GaAsP photon counting PMT (H7422, Hamamatsu) connected to a time correlated single photon counting (TCSPC) system (SPC-730, Becker & Hickl).

All *in vivo* multiphoton FLIM images were collected with a second system constructed around a Nikon Diaphot 200 microscope (20). The excitation source is a titanium-sapphire laser (Coherent, Mira; 76 MHz, 120 fs) pumped by an 8 W solid-state laser (Coherent, Verdi). Other components include a 60x oil immersion objective (Nikon, PlanApo NA=1.4), and a dichromatic mirror (650DCSP, Chroma, Inc., Rockingham, VT) to reflect the 780 nm excitation light onto the sample and transmit wavelengths between 400 nm and 650 nm to the detector. FLIM data were collected pixel-by-pixel with a laser scanning unit (BioRad, MRC-600), a fast photon-counting

PMT (Becker & Hickl, PMH-100), and TCSPC electronics (Becker & Hickl, SPC-830). To control the power coupled to the system, a variable neutral density filter wheel was positioned before the entrance to the scanning unit. Acquisition for both systems was done with WiscScan (21), a lab developed software package.

Cell Culture Perturbation Experiments

MCF10A cells were obtained from the American Type Culture Collection (22). The cells remained free of Mycoplasma and other contaminants and were propagated by adherent culture according to established protocols (23). MCF10A cells were grown in DMEM-F12 supplemented with 5% horse serum, 20 ng/mL epidermal growth factor, 10 μg/mL insulin, and 0.5 mg/mL hydrocortisone. Plated cells were stored in a 10% CO_2 incubator at 37^oC and cultured every 3 to 4 days. Cells were detached from the flasks by trypsinization and triply washed in 10 mL of PBS. A hemacytometer was used to determine the concentration of the cells by counting the number of cells per milliliter. Upon determination of the concentration of the cells, the volumes required to plate 25,000 and 1,000,000 cells per dish were calculated, respectively. MCF10A cells at the two different densities were plated on lysine coated cover glass bottom Petri dishes (size, 35 mm; P35G-0-41-C, MatTek, Ashland, MA) and immersed in their standard growth media. Two different cell concentrations were used for these experiments because previous work has shown that the lifetime of NADH in cell culture depends on the cell confluency (due to changes in metabolism with cell confluency) (24).

Redox ratio images (25), which are defined as the fluorescence intensity of FAD divided by the sum of the fluorescence intensities of FAD and NADH, can be used to estimate the oxidation-reduction state of cells. Redox ratio imaging was used to verify that the concentrations and incubation times of 3-bromopyruvate and $CoCl_2$ produced changes in cellular metabolism. Cells were either left untreated (control), treated with 300 μM 3-bromopyruvate (Sigma-Aldrich, St. Louis, MO) for 60 to 90 minutes to inhibit glycolysis, or treated with 200 μM $CoCl_2$ (Sigma-Aldrich, St. Louis, MO) for 60 to 90 minutes to inhibit oxidative phosphorylation, as verified by changes in the redox ratio. NADH lifetime and intensity images were collected at a two-photon excitation wavelength of 780 nm and FAD intensity images were collected at 890 nm excitation, (26). At the completion of the final image acquisition, cell viability was confirmed under light microscopy (using the same microscope) by trypan blue exclusion. All cell dishes remained viable throughout any given imaging session.

The average peak power for the cell imaging experiments was approximately 15 mW. Single photon counting was done at a rate of approximately 500 x 10^5 photons/s for 60 seconds with a pixel dwell time of approximately 11.5 μs. The scan area at each image plane was 256x256 pixels (140x140 μm). Photon count rates at the beginning and end of image acquisition were monitored to ensure that photobleaching did not occur. The instrument response function (IRF) was measured using a second harmonic generated signal from a β-BaB_2O_4 crystal (20). The full width at half maximum (FWHM) of the IRF was 0.313 ns for the cell culture experiments. This represents the IRF of the *overall* system where the components that mainly contribute to temporal degradation are the transient time spread of the detector, optical dispersion at mirrors and through lenses, and light scattering at diaphragms.

DMBA-Treated Hamster Cheek Pouch Model of Oral Cancer

A total of 13 DMBA-treated and 9 control male Golden Syrian hamsters were evaluated in this study (average weight: 156 ± 13 g). Animal care and procedures were in accordance with the guidelines in the U.S. Department of Health and Human Services and National Institutes of Health "Guide for the Care and Use of Laboratory Animals" and approved by the Institutional Animal Care and Use Committee at the University of Wisconsin. For each hamster, the right cheek pouch was either treated three times per week with 0.5% DMBA (by weight) in mineral oil (DMBA-treated animals), or the right cheek pouch was treated at the same frequency with mineral oil only (control animals) for a total of 16 weeks. The treatment schedule and procedures were established from previous studies (27, 28). At 16-21 weeks after the commencement of DMBA or mineral oil treatment, the cheek pouch of each animal was imaged using multiphoton FLIM at an excitation wavelength of 780 nm, which falls within the absorption band of NADH (26). This wavelength was also selected because statistically significant differences in tissue fluorescence intensity have been observed between normal tissues, dysplasias and carcinomas in the hamster cheek pouch model with multiphoton microscopy at a two-photon excitation wavelength of 780 nm (28).

Prior to imaging, each hamster was anesthetized with an intra-peritoneal injection of a mixture of 2.5 mg/kg acepromazine, 200 mg/kg ketamine, and 5 mg/kg xylazine. Next, the cheek pouch was inverted and stretched over an 8 mm diameter cork, pinned to the sides of the cork with two 27-gauge needles, and then wiped with saline. A cover slip was secured on the objective side of a 10 mm diameter opening in the imaging stage using Vaseline. The animal was placed on its stomach, and the cork was secured to the imaging stage of the inverted microscope such that the cheek was flush against the cover slip. The microscope objective was centered within the 10 mm opening of the imaging stage prior to image collection.

The average power incident on the sample ranged from approximately 3.3 – 7.2 mW. Single photon counting was done at a rate of approximately 500 x 10^5 photons/s for 45 seconds to 5 minutes with a pixel dwell time of approximately 6.25 μs. The scan area at each image plane was 256x256 pixels (140x140 μm). Photon count rates at the beginning and end of image acquisition were monitored to ensure that photobleaching did not occur. The image z-stacks were generated using a 10 μm z-step size.

To ensure instrument consistency between experimental days, the lifetime of a known and stable instrument standard, 20 μm diameter Fluoresbrite YG (yellow green) microspheres (Polysciences Inc.) was imaged at the beginning of each day of the *in vivo* experiments (n=14). The microspheres were measured under the same experimental conditions as the *in vivo* measurements, except the power at the sample and the integration time were adjusted to achieve a single photon count rate of approximately 500 x 10^5 from the significantly brighter microspheres. The lifetime decay curves measured from the microspheres were fit to a single exponential decay model using SPCImage software (see below). The average lifetime for the microspheres (n=14) was 2.13 ± 0.11 ns. The measured value for the lifetime of these spheres is consistent with that reported in other studies (~2.2 ± 0.1 ns) (24, 29). The IRF measured using a second harmonic generated signal from a β-BaB_2O_4 crystal had a FWHM of 0.190 ± 0.002 ns for the *in vivo* experiments. The IRF for the *in vivo* experiments differs from that of the cell culture experiments due to different detectors and optical paths in the two multiphoton FLIM systems.

After *in vivo* imaging, a biopsy was taken from the imaged site (center of the 10 mm stage opening) with a 3 mm diameter dermal biopsy punch. The biopsy was placed in 10% buffered formalin and submitted for histopathology. The tissue biopsies were cut and stained with hematoxylin and eosin (H&E), and read by a board certified veterinary pathologist (Annette Gendron-Fitzpatrick). Diagnosis was based on established criteria (30), with tissues assigned to one of the following categories: normal, hyperplasia, mild dysplasia, moderate dysplasia, severe dysplasia, papillary hyperplasia / papilloma, carcinoma *in situ* (CIS), or squamous cell carcinoma (SCC). The diagnosis for a given biopsy was determined from an evaluation of multiple sections cut from that biopsy. If any of these tissue biopsies were found to have more than one diagnosis (for example, severe dysplasia and SCC), the most severe diagnosis was assigned to that biopsy. FLIM images were taken from a microscopic field of view (140x140 μm), thus it was difficult to mark the precise image site on the biopsy. The approach taken in this study was to assign a diagnosis to each image stack based on the most severe pathologic diagnosis of the entire corresponding biopsy sample. This approach was consistent with that reported in our previous study which employed multiphoton microscopy to characterize the NADH intensity in the hamster cheek pouch model of carcinogenesis (28).

Analysis of the Fluorescence Lifetime Decay Curves

SPCImage software (Becker & Hickl) was used to analyze the fluorescence lifetime decay curves (24). First, the measured instrument response was deconvolved from the measured lifetime decay curve for a given pixel. Next, the deconvolved lifetime decay curve was binned over the pixel of interest and the 8 nearest neighbor pixels. This produced a lifetime decay curve with a peak value of approximately 100 counts. The lifetime decay curve of the pixel of interest was then fit to a double-exponential decay model shown below.

$$F(t) = \alpha_1 e^{-t/\tau_1} + \alpha_2 e^{-t/\tau_2}$$

F(t) is the fluorescence intensity at time t after the excitation light has ceased, τ_1 and τ_2 are the fluorophore lifetimes (τ_1 is the short lifetime component and τ_2 is the long lifetime component), and α_1 and α_2 are the relative contributions of the lifetime components (i.e. $\alpha_1 + \alpha_2 = 100\%$). The lifetime for the pixel of interest was calculated by finding the global minimum of the χ^2 value. The minimum calculated lifetime constrained by the fit model in SPCImage was 0.1 ns, which is close to the temporal response of the multiphoton FLIM system. The mean and standard deviation of the χ^2 value (a χ^2 value close to one indicates a good fit) for the entire field of view of all *in vivo* hamster cheek pouch images and *in vitro* cell culture image planes was 1.05 ± 0.05 and 1.01 ± 0.01, respectively. A survey of χ^2 values on a few samples indicated that the double-exponential decay model improved the χ^2 value of the fit over the single-exponential decay model, and the triple-exponential decay model did not improve the χ^2 value of the fit compared to the double-exponential decay model. The presence of two distinctly different lifetimes for free and protein-bound NADH (8, 31) also indicates that NADH fluorescence decay curves are best fit to a double-exponential decay model.

Simulated fluorescence lifetime decay curves indicate that the τ_1, τ_2, α_1, and α_2 recovered with SPCImage from high SNR decay curves are accurate to within 1%, and results achieved from simulated lifetime decay curves with an SNR similar to the measured *in vivo* and *in vitro* lifetime decay curves are accurate to within 6%.

Quantification of Variables from the FLIM Images for Statistical Analyses

Cell culture: All FLIM and fluorescence intensity images at a given cell density (low or high) were obtained on the same day (for a total of two experimental days, one for each of the two cell densities). For the analysis of cell culture lifetime images, the region of interest (ROI) containing the cells was selected, and the fluorescence intensity threshold in SPCImage was adjusted so that signals from the nucleus were below the threshold. The region of interest included as few as 2 cells (low cell density) or as many as 60 cells (high cell density). Next, the lifetimes of all pixels in the region of interest were calculated, and the mean value of τ_1, τ_2, and α_2 were recorded for each of the three ROI per dish. The redox ratio [fluorescence intensity of FAD/(FAD+NADH)] was calculated from the mean intensity of the 890 nm excitation images (FAD) and the mean intensity of the corresponding 780 nm excitation images (NADH). The mean redox ratio was recorded for each of the three regions of interest per dish. All redox ratio images at a given cell density were collected under identical experimental conditions on the same day. High density cells included control cells (n=8 total ROI from 4 dishes), cells treated with 3-bromopyruvate (n=6 total ROI from 2 dishes), and cells treated with $CoCl_2$ (n=6 total ROI from 2 dishes). Low density cells included control cells (n=5 total ROI from 2 dishes), cells treated with 3-bromopyruvate (n=6 total ROI from 2 dishes), and cells treated with $CoCl_2$ (n=6 total ROI from 2 dishes).

Hamster cheek pouch model: The epithelium and stroma were analyzed separately by choosing volumes of interest based on morphology. For the analysis of the epithelial layer, three cells were randomly chosen in each image plane within a depth stack of multiple image planes within an animal. The fluorescence intensity threshold in SPCImage was adjusted so that signals from the nucleus were below the threshold, and the lifetimes were calculated per pixel from all pixels within each cell. Separate matrices for τ_1, τ_2, and α_2 for each cell were exported to Matlab (The Mathworks, Inc., Natick, MA). Then the mean and standard deviation of each of these parameters was calculated for each cell. The nuclear diameter was measured in an arbitrary orientation for the same set of cells for which the lifetime analysis was performed. The epithelial layer thickness was measured by counting the number of image planes (10 μm z-steps) between the first layer of epithelial cells and the first layer in which fibrillar collagen was observed, or the working distance of the objective was reached.

In the stromal layer, the lifetime was averaged for the entire field of view (256 x 256 pixels) of one image plane containing collagen fibrils within the cheek pouch of each animal.

Changes in cellular lifetime with depth in the epithelium within an animal were evaluated by averaging all three cells within an image plane and using *paired* non-parametric Wilcoxon Signed Rank tests to compare the first and last plane in the epithelium within an animal. All cells within an animal were averaged to perform comparisons between disease states using *unpaired* non-parametric Wilcoxon Rank-Sum tests. The cellular coefficient of variation (cell standard deviation / cell mean) was calculated for each cell as a measure of intracellular variability (32), and comparisons of all cells across disease states were made using both unpaired Wilcoxon Rank-Sum tests and unpaired t-tests. Exact p-values were computed, all p-values are two-sided, and a p-value of < 0.05 was considered statistically significant. Parametric methods (linear mixed effects models with log-transformed outcome variables) were used for validation purposes and led to similar results. SAS version 6.12 (Cary, NC) and Matlab (The Mathworks, Inc., Natick, MA) were used for all statistical analyses.

Results

Cell Culture Perturbation Studies

Pertubation with 3-bromopyruvate produced a statistically significant increase in the redox ratio and $CoCl_2$ produced a statistically significant decrease in the redox ratio, reflecting an alteration in the metabolism with these perturbations (Table 1 (a) and (b)). The results for high density and low density cells are separated because previous work has shown that the cellular lifetime of NADH depends on the cell confluency (due to changes in metabolism with cell confluency) (24). The fluorescence lifetimes at 780 nm excitation ($\tau_1 = 0.30 \pm 0.03$ ns and $\tau_2 = 2.40 \pm 0.07$ ns, averaged for control cells at low and high cell densities) are consistent with free and protein-bound NADH, respectively (8, 31). The fluorescence lifetimes at 890 nm excitation ($\tau_1 = 0.15 \pm 0.01$ ns, $\tau_2 = 2.44 \pm 0.06$ ns, $\alpha_2 = 17 \pm 2$ %, averaged for control cells at low and high cell densities) are consistent with FAD fluorescence (33). The focus of these experiments is changes in protein-bound NADH with metabolic perturbations, so the statistical analysis of the lifetime of free NADH (τ_1) is not shown. Perturbation with 3-bromopyruvate caused an increase in the fluorescence lifetime of protein-bound NADH (τ_2) and a decrease in the relative contribution of protein-bound NADH to the overall lifetime decay (α_2) in cells plated at both low and high densities (Table 1 (a) and (b), $p<0.05$). Perturbation with $CoCl_2$ caused a decrease in the fluorescence lifetime of protein-bound NADH (τ_2) and a decrease in α_2 in cells plated at low and high cell densities (Table 1 (a) and (b), $p<0.05$).

Hamster Cheek Pouch Pathology

Histopathology was used as the gold standard for tissue diagnosis. Of the 22 cheek pouches imaged (one per animal), 9 were diagnosed as normal (the 9 control animals), and of the 13 DMBA-treated animals 2 were diagnosed with mild dysplasia, 4 with moderate dysplasia, 4 with severe dysplasia, 2 with CIS and 1 with SCC. For the purpose of statistical analyses, the tissue samples were divided into three categories: normal (n=9), low grade pre-cancer (mild dysplasia and moderate dysplasia, n=6) and high grade pre-cancer (severe dysplasia and CIS, n=6). High grade pre-cancers are more likely to progress to cancer than low grade pre-cancers (34). The single SCC sample was not included in the statistical analysis.

Multiphoton FLIM Images of Normal, Pre-Cancerous and Cancerous Tissue in vivo

The hamster cheek pouch has three distinct layers: an acellular superficial layer, an epithelium and an underlying stroma. Three-dimensional image stacks of fluorescence lifetimes and the fractional contribution of the long lifetime component of these different layers (Figure 1) were used to determine whether multiphoton FLIM can differentiate histologically confirmed normal and dysplastic tissues.

In the normal cheek pouch (Figs. 1 (a-c)), the acellular superficial layer fluorescence (0 μm) has a fairly uniform distribution of long lifetime contribution (α_2), short lifetime (τ_1), and long lifetime (τ_2). However, in low-grade (Fig. 1 (d)) and high grade pre-cancers, (Fig. 1 (e)), the τ_2 of the superficial layer is non-uniform. There was no acellular superficial layer in the one SCC sample (Fig. 1 (f)). The cytoplasmic fluorescence of the cells in the epithelium of the normal cheek pouch (Fig. 1 (a-c), between 10 - 30 μm depths) has a short (τ_1) and long (τ_2) lifetime component consistent with free and protein-bound NADH, respectively (8, 31) (percent contribution of protein-bound NADH, α_2). The nuclear to cytoplasmic ratio of the cells increases with depth in the epithelium. However, this trend is not observed in the high grade pre-cancer (Fig. 1 (e)) or the SCC (Fig. 1 (f)). The cellular fluorescence distribution in the high grade pre-cancer and SCC is also more perinuclear compared to normal tissue. The predominant lifetime component in the normal and pre-cancerous epithelial cells is τ_1. τ_2 of pre-cancerous and cancerous cells appears to be shorter than normal cells. The lifetime of structural proteins in the stromal layer is much different than the lifetime of NADH in the epithelial cells. In the stromal layer of the normal cheek pouch (Fig. 1 (a-c), 40 μm depth) τ_1 is the predominant lifetime component (the contribution of τ_2 is negligible) and its value is similar to the temporal response of the FLIM system and thus is attributed to the second harmonic generation (SHG) of fibrillar collagen (which has a zero lifetime (35)). The stromal layer in the pre-cancers and SCC is at a much greater depth than 40 μm.

Statistical Analyses of Fluorescence Lifetime Parameters

Features that were qualitatively observed to change with pre-cancer development in the multiphoton FLIM images were next quantified to determine if these observed differences were statistically significant. First, morphological variables were quantified, and statistical tests revealed that the epithelial thickness of high grade pre-cancers (52 ± 8 μm) are greater than normal (18 ± 2 μm), and the nuclear diameter of low grade (7.5 ±

0.5 μm) and high grade (7.5 ± 0.4 μm) pre-cancers are greater than normal (6.3 ± 0.3 μm) ($p<0.05$).

The range of τ_1 in normal tissue was 0.29 ± 0.03 ns (consistent with free NADH). The focus of this study is changes in protein-bound NADH with pre-cancer development, so the statistical analysis of the lifetime of free NADH (τ_1) is not shown.

Changes in cellular lifetime with depth in the epithelium are shown in Figure 2. Paired statistical tests revealed no change in cellular τ_2 or α_2 with depth within the epithelium of normal tissues and high grade pre-cancers ($p>0.05$). However, cellular τ_2 and α_2 were found to decrease with depth within the epithelium of low grade pre-cancers ($p<0.05$).

Statistical tests also revealed that normal and dysplastic tissues are differentiated with the mean cellular τ_2 (Table 2). The τ_2 of both low grade and high grade pre-cancers are statistically lower than normal ($p<0.05$). The α_2 of low grade pre-cancers is also statistically lower than normal.

Intracellular variability was assessed with the cellular coefficient of variation (32) (Figure 3). Intracellular τ_2 and α_2 variability for high grade and low grade pre-cancers is statistically greater than normal ($p<0.05$), and intracellular α_2 variability for low grade pre-cancers is statistically greater than high grade pre-cancers ($p<0.05$).

The mean α_2 (1.5 ± 0.6 %) and τ_1 (0.10 ± 0.003 ns) of normal and dysplastic collagen confirms that the collagen signal is 99% SHG (which has zero lifetime (35), the minimum calculated lifetime constrained by the fit model is 0.1 ns).

Discussion

The results of this study indicate that multiphoton FLIM provides structural (cellular-level morphology in three spatial dimensions) and metabolic (NADH lifetime) information that discriminates between normal tissue and pre-cancers *in vivo*. The morphological differences identified with pre-cancer development (increased nuclear diameter and epithelial thickness) are consistent with a previous multiphoton microscopy study of the DMBA-treated hamster cheek pouch (28). These morphological changes are also consistent with previous histopathology studies (16, 30, 36). However, multiphoton FLIM has the advantage of resolving these structural differences *in vivo* without the need for physical sectioning, and providing functional images of tissue metabolism with the NADH fluorescence lifetime. The protein-bound NADH fluorescence lifetime discriminated normal vs. high grade and normal vs. low grade pre-cancers *in vivo* (Table 2). The amount of protein-bound NADH relative to free NADH (α_2) also decreased with low grade pre-cancer compared to normal (Table 2).

Cell culture perturbation studies (Table 1) revealed that the protein-bound NADH lifetime component (τ_2) increases with the addition of 3-bromopyruvate and decreases with the addition of $CoCl_2$ (consistent with previous work (24, 31, 37)), and these lifetime changes increase and decrease with the redox ratio. It is expected that the addition of 3-bromopyruvate causes inhibition of glycolysis, thus resulting in an increase in the redox ratio while $COCl_2$ causes inhibition of oxidative phosphorylation thus decreasing the redox ratio in cell culture. These perturbation studies suggest that the NADH lifetime is sensitive to metabolic changes, but unlike the redox ratio, NADH lifetime measurements can be made at a single excitation wavelength without corrections for excitation energy exposure or throughput of the system.

The short lifetime component (τ_1) and long lifetime component (τ_2) of the normal epithelial cells measured *in vivo* in the hamster cheek pouch are within the range of published values of free NADH and protein-bound NADH, respectively, in cell culture, tissue slices and *in vivo* tissue (8, 31, 37-39). However, the published lifetimes of free and protein-bound NADH vary widely depending on the biological system investigated. It is also possible that flavin adenine dinucelotide (FAD) could contribute to the measured lifetime at a two-photon excitation wavelength of 780 nm. However, *in vivo* multiphoton fluorescence images collected at 900 nm excitation (optimal for the two-photon excitation of FAD (26)) did not show any measurable fluorescence, indicating that FAD is unlikely to contribute to the observed lifetime at 780 nm excitation in the hamster cheek pouch. Another source of fluorescence at this excitation wavelength is NADPH. Previous studies have shown that the concentration of NADH is about 5 times greater than NADPH (40), the NADH quantum yield is 1.25 – 2.5 times greater than NADPH (41), and metabolic perturbations produce fluorescence changes dominated by NADH (42). Thus, its likely that NADPH is responsible for a low, relatively constant fluorescence background in these studies (37).

Normal and pre-cancerous tissues were differentiated with the protein-bound NADH lifetime (τ_2), with low grade and high grade pre-cancerous tissues having a lower τ_2 than normal (Table 2). The Warburg effect predicts that neoplasias favor glycolysis over oxidative phosphorylation under aerobic conditions (6, 7), and given the results of the cell perturbation study (Table 1), the measured decrease in protein-bound NADH lifetime with neoplasia is consistent with increased levels of glycolysis. This shift to glycolysis could be due to either the Warburg effect or the Pasteur effect (43), which is increased glycolysis due to hypoxia. Changes in the distribution of NADH enzyme binding sites associated with preferred metabolic pathways in neoplastic tissues (10) may be responsible for the change in protein-bound NADH lifetime with pre-cancer. However, further studies are required to test this hypothesis.

Increased intracellular τ_2 and α_2 variability were observed in pre-cancerous tissues, and low grade pre-cancers had increased intracellular α_2 variability compared to high grade pre-cancers (Fig. 3). This could be due to heterogeneous NADH binding and microenvironments within the cells. FLIM studies of pre-cancerous cells *in vivo* at higher magnifications with perturbations to cytosolic and mitochondrial metabolism could further investigate the heterogeneity of lifetimes within individual cells.

The lifetime of low grade pre-cancers was found to decrease with depth in the epithelium, while the lifetime of normal and high grade pre-cancers did not change with depth. Neoplastic cells originate near the basement membrane and can move progressively upward through the epithelium (9). In a low grade pre-cancer, the epithelium is only partially occupied by the less differentiated neoplastic cells, while in a high-grade pre-cancer the full thickness of the epithelium is occupied by these cells (44). It may be speculated that increased heterogeneity in cell populations in low grade pre-cancers may be partly responsible for the variation in lifetime with depth in these tissues.

Multiphoton FLIM is ideal for pre-cancer detection in squamous epithelial tissues because the penetration depth of multiphoton FLIM (dependent on the optical properties of the organ site, but up to 0.3 mm in human skin (45), for example) is comparable to the thickness of the epithelium in a variety of tissues including the cervix and oral cavity (46). Multiphoton FLIM could also be used for other clinical applications, including non-invasive glucose monitoring in diabetics (47) and metabolic monitoring for tumor therapy. In the near-term, the important findings from multiphoton FLIM studies could guide the design and development of practical time-gated fluorescence detection schemes for clinical applications. In long-term, portable technology could be engineered to enable multiphoton FLIM in a clinical setting.

Acknowledgements: The authors would also like to thank John White, Axel Bergmann, and Jayne Squirrell for their scientific input, and Kristin Vrotsos and Paolo Provenzano for their help with animal and cell culture experiments, respectively. This work was supported by the National Institutes of Health (R01 EB000184) and the Department of Defense, Predoctoral Traineeship Award W81XWH-04-1-0330 (for M.S.).

References

1. K. Suhling, P. M. French and D. Phillips, "Time-resolved fluorescence microscopy," Photochem Photobiol Sci 4(1), 13-22 (2005)
2. J. R. Lakowicz, Principles of Fluorescence Spectroscopy, Plenum Publishers, New York (1999).
3. W. Denk, J. H. Strickler and W. W. Webb, "Two-photon laser scanning fluorescence microscopy," Science 248(4951), 73-76 (1990)
4. V. E. Centonze and J. G. White, "Multiphoton excitation provides optical sections from deeper within scattering specimens than confocal imaging," Biophys J 75(4), 2015-2024 (1998)
5. J. M. Squirrell, D. L. Wokosin, J. G. White and B. D. Bavister, "Long-term two-photon fluorescence imaging of mammalian embryos without compromising viability," Nat Biotechnol 17(8), 763-767 (1999)
6. C. J. Gulledge and M. W. Dewhirst, "Tumor oxygenation: a matter of supply and demand," Anticancer Res 16(2), 741-749 (1996)
7. O. Warburg, The Metabolism of Tumors, Constabel, London (1930).
8. J. R. Lakowicz, H. Szmacinski, K. Nowaczyk and M. L. Johnson, "Fluorescence lifetime imaging of free and protein-bound NADH," Proc Natl Acad Sci U S A 89(4), 1271-1275 (1992)
9. B. Alberts, A. Johnson, J. Lewis, M. Raff, K. Roberts and P. Walter, Molecular Biology of the Cell, Garland Science, New York (2002).
10. S. Banerjee and D. K. Bhatt, "Histochemical studies on the distribution of certain dehydrogenases in squamous cell carcinoma of cheek," Indian J Cancer 26(1), 21-30 (1989)
11. I. Iweibo, "Protein fluorescence and electronic energy transfer in the determination of molecular dimensions and rotational relaxation times of native and coenzyme-bound horse liver alcohol dehydrogenase," Biochim Biophys Acta 446(1), 192-205 (1976)
12. A. R. Jones, L. Gillan and D. Milmlow, "The anti-glycolytic activity of 3-bromopyruvate on mature boar spermatozoa in vitro," Contraception 52(5), 317-320 (1995)
13. A. W. Lee and D. J. States, "Colony-stimulating factor-1 requires PI3-kinase-mediated metabolism for proliferation and survival in myeloid cells," Cell Death Differ (2006)
14. N. S. Chandel, E. Maltepe, E. Goldwasser, C. E. Mathieu, M. C. Simon and P. T. Schumacker, "Mitochondrial reactive oxygen species trigger hypoxia-induced transcription," Proc Natl Acad Sci U S A 95(20), 11715-11720 (1998)
15. E. Hervouet, P. Pecina, J. Demont, A. Vojtiskova, H. Simonnet, J. Houstek and C. Godinot, "Inhibition of cytochrome c oxidase subunit 4 precursor processing by the hypoxia mimic cobalt chloride," Biochem Biophys Res Commun 344(4), 1086-1093 (2006)
16. F. H. White, K. Gohari and C. J. Smith, "Histological and ultrastructural morphology of 7,12 dimethylbenz(alpha)-anthracene carcinogenesis in hamster cheek pouch epithelium," Diagn Histopathol 4(4), 307-333 (1981)

17. S. Andrejevic, J. F. Savary, C. Fontolliet, P. Monnier and H. van Den Bergh, "7,12-dimethylbenz[a]anthracene-induced 'early' squamous cell carcinoma in the Golden Syrian hamster: evaluation of an animal model and comparison with 'early' forms of human squamous cell carcinoma in the upper aero-digestive tract," Int J Exp Pathol 77(1), 7-14 (1996)
18. C. T. Chen, H. K. Chiang, S. N. Chow, C. Y. Wang, Y. S. Lee, J. C. Tsai and C. P. Chiang, "Autofluorescence in normal and malignant human oral tissues and in DMBA-induced hamster buccal pouch carcinogenesis," J Oral Pathol Med 27(10), 470-474 (1998)
19. D. L. Wokosin, J. M. Squirrell, K. W. Eliceiri and J. G. White, "An optical workstation with concurrent independent multiphoton imaging and experimental laser microbeam capabilities," Rev Sci Instrum 74(1), (2003)
20. D. K. Bird, K. W. Eliceiri, C. H. Fan and J. G. White, "Simultaneous two-photon spectral and lifetime fluorescence microscopy," Appl Opt 43(27), 5173-5182 (2004)
21. M. Z. Nazir, K. W. Eliceiri, A. Ahmed, A. Hashmi, V. Agarwal, Y. Rao, S. Kumar, T. Lukas, M. Nasim, C. Rueden, R. Gunawan and J. G. White, "WiscScan: A Software Defined Laser-Scanning Microscope," Scanning Submitted((2006)
22. http://www.atcc.org,
23. P. J. Keely, A. M. Fong, M. M. Zutter and S. A. Santoro, "Alteration of collagen-dependent adhesion, motility, and morphogenesis by the expression of antisense alpha 2 integrin mRNA in mammary cells," J Cell Sci 108 (Pt 2)(595-607 (1995)
24. D. K. Bird, L. Yan, K. M. Vrotsos, K. W. Eliceiri, E. M. Vaughan, P. J. Keely, J. G. White and N. Ramanujam, "Metabolic mapping of MCF10A human breast cells via multiphoton fluorescence lifetime imaging of the coenzyme NADH," Cancer Res 65(19), 8766-8773 (2005)
25. B. Chance, B. Schoener, R. Oshino, F. Itshak and Y. Nakase, "Oxidation-reduction ratio studies of mitochondria in freeze-trapped samples. NADH and flavoprotein fluorescence signals," J Biol Chem 254(11), 4764-4771 (1979)
26. S. Huang, A. A. Heikal and W. W. Webb, "Two-photon fluorescence spectroscopy and microscopy of NAD(P)H and flavoprotein," Biophys J 82(5), 2811-2825 (2002)
27. M. C. Skala, G. M. Palmer, C. Zhu, Q. Liu, K. M. Vrotsos, C. L. Marshek-Stone, A. Gendron-Fitzpatrick and N. Ramanujam, "Investigation of fiber-optic probe designs for optical spectroscopic diagnosis of epithelial pre-cancers," Lasers Surg Med 34(1), 25-38 (2004)
28. M. C. Skala, J. M. Squirrell, K. M. Vrotsos, J. C. Eickhoff, A. Gendron-Fitzpatrick, K. W. Eliceiri and N. Ramanujam, "Multiphoton microscopy of endogenous fluorescence differentiates normal, precancerous, and cancerous squamous epithelial tissues," Cancer Res 65(4), 1180-1186 (2005)
29. A. Schonle, M. Glatz and S. W. Hell, "Four-dimensional multiphoton microscopy with time-correlated single-photon counting," Applied Optics 39(34), 6306-6311 (2000)
30. D. G. MacDonald and S. M. Saka, Structural Indicators of the High Risk Lesion, Cambridge Univ. Press, Cambridge (1991).
31. H. Schneckenburger, M. Wagner, P. Weber, W. S. L. Strauss and R. Sailer, "Autofluorescence lifetime imaging of cultivated cells using a UV picosecond laser diode," J. Fluorescence 14(649-654 (2004)

32. J. Gibbons and S. Chakraborti, Nonparametric Statistical Inference, Marcel Dekker, New York (1992).

33. F. Tanaka, N. Tamai and I. Yamazaki, "Picosecond-resolved fluorescence spectra of D-amino-acid oxidase. A new fluorescent species of the coenzyme," Biochemistry 28(10), 4259-4262 (1989)

34. G. F. Sawaya, A. D. Brown, A. E. Washington and A. M. Garber, "Clinical practice. Current approaches to cervical-cancer screening," N Engl J Med 344(21), 1603-1607 (2001)

35. P. J. Campagnola and L. M. Loew, "Second-harmonic imaging microscopy for visualizing biomolecular arrays in cells, tissues and organisms," Nat Biotechnol 21(11), 1356-1360 (2003)

36. Y. V. Xiang, "[Quantitative study on esophageal cytology. I. Quantitative morphologic studies of normal, dysplastic and malignant squamous cells]," Zhonghua Zhong Liu Za Zhi 12(2), 92-94 (1990)

37. H. D. Vishwasrao, A. A. Heikal, K. A. Kasischke and W. W. Webb, "Conformational dependence of intracellular NADH on metabolic state revealed by associated fluorescence anisotrophy," J Biol Chem (2005)

38. R. Niesner, B. Peker, P. Schlusche and K. H. Gericke, "Noniterative biexponential fluorescence lifetime imaging in the investigation of cellular metabolism by means of NAD(P)H autofluorescence," Chemphyschem 5(8), 1141-1149 (2004)

39. K. Konig and I. Riemann, "High-resolution multiphoton tomography of human skin with subcellular spatial resolution and picosecond time resolution," J Biomed Opt 8(3), 432-439 (2003)

40. L. K. Klaidman, A. C. Leung and J. D. Adams, Jr., "High-performance liquid chromatography analysis of oxidized and reduced pyridine dinucleotides in specific brain regions," Anal Biochem 228(2), 312-317 (1995)

41. Y. Avi-Dor, J. Olson, M. Doherty and N. Kaplan, "Fluorescence of Pyridine Nucleotides in Mitochondria," J Biol Chem 237(7), 2377-2383 (1962)

42. B. Chance, J. Williamson, D. Jamieson and B. Schoener, "Properties and kinetics of reduced pyridine nucleotide fluorescence of the isolated and in vivo rat heart," Biochem Z 341(357-377 (1965)

43. T. Schroeder, H. Yuan, B. L. Viglianti, C. Peltz, S. Asopa, Z. Vujaskovic and M. W. Dewhirst, "Spatial heterogeneity and oxygen dependence of glucose consumption in R3230Ac and fibrosarcomas of the Fischer 344 rat," Cancer Res 65(12), 5163-5171 (2005)

44. I. Pavlova, K. Sokolov, R. Drezek, A. Malpica, M. Follen and R. Richards-Kortum, "Microanatomical and biochemical origins of normal and precancerous cervical autofluorescence using laser-scanning fluorescence confocal microscopy," Photochem Photobiol 77(5), 550-555 (2003)

45. P. T. So, C. Y. Dong, B. R. Masters and K. M. Berland, "Two-photon excitation fluorescence microscopy," Annu Rev Biomed Eng 2(399-429 (2000)

46. D. H. Cormack, Clinically Integrated Histology, Lipincott-Rave, Philadelphia, PA (1998).

47. N. D. Evans, L. Gnudi, O. J. Rolinski, D. J. Birch and J. C. Pickup, "Glucose-dependent changes in NAD(P)H-related fluorescence lifetime of adipocytes and

fibroblasts in vitro: potential for non-invasive glucose sensing in diabetes mellitus," J Photochem Photobiol B 80(2), 122-129 (2005)

Figure and Table Legends

Table 1: Cell culture NADH fluorescence lifetimes and redox ratios. Mean and standard deviation of τ_2 (protein-bound NADH lifetime), α_2 (percent contribution of protein-bound NADH) and the redox ratio [fluorescence intensity of FAD/(NADH+FAD)] for (a) high density control cells (n=8 images from 4 dishes), cells treated with 3-bromopyruvate (n=6 images from 2 dishes), which inhibits glycolysis, and cells treated with $CoCl_2$ (n=6 images from 2 dishes), which inhibits oxidative phosphorylation. Mean and standard deviation of τ_2, and α_2 for (b) low density control cells (n=5 images from 2 dishes), cells treated with 3-bromopyruvate (n=6 images from 2 dishes), and cells treated with $CoCl_2$ (n=6 images from 2 dishes). Statistically significant differences ($p<0.05$, unpaired Wilcoxon Rank-Sum Tests) exist between control vs. 3-bromopyruvate treated and control vs. $CoCl_2$ treated cells for the variables marked with an asterisk (*). The excitation wavelength is 780 nm, and the cells are MCF10A breast epithelial cells.

Figure 1: Multiphoton FLIM of the normal hamster cheek pouch (a, b, c), low grade pre-cancer (d, mild dysplasia), high grade pre-cancer (e, severe dysplasia), and SCC (f) measured *in vivo* at 780 nm excitation. Images are color coded to values of α_2 (contribution of long lifetime component; a), τ_1 (short lifetime component; b), and τ_2 (long lifetime component; c, d, e, f). The color bar range is at the bottom of each montage. Note that τ_1, τ_2 and α_2 each have a different color scale, and the color scale for (f) is different than (c, d, e). The numbers in the lower left corner of each image

indicate the depth below the tissue surface in microns, and each image is 100 μm x 100 μm.

Figure 2: Percent change in τ_2 (protein-bound NADH lifetime; a) and α_2 (percent contribution of protein-bound NADH; b) with depth within the epithelium of the hamster cheek pouch *in vivo*. Within each animal, τ_2 and α_2 of three cells per image plane were averaged, and then the percent changes in τ_2 and α_2 of each plane were calculated relative to those of the most superficial plane in the epithelium (defined as the first layer of cells below the acellular superficial layer). Next, the percent change in τ_2 and α_2 at each depth were averaged for all animals. Solid circles represent the mean percent change for the last plane of the epithelium for all animals, plotted at the mean depth of the last plane in the epithelium of all animals relative to the most superficial plane in the epithelium. Paired Wilcoxon Signed Rank Tests of the first vs. last plane in the epithelium within an animal indicated a statistically significant decrease in τ_2 and α_2 with depth ($p<0.05$) in low-grade pre-cancers.

Table 2: *In vivo* NADH fluorescence lifetimes. Mean and standard deviation of τ_2 (protein-bound NADH lifetime) and α_2 (percent contribution of protein-bound NADH) averaged for all cells within an animal for all normal animals (n=9), low grade pre-cancerous animals (n=6) and high grade pre-cancerous animals (n=6). Statistically significant differences ($p<0.05$, unpaired Wilcoxon Rank-Sum Tests) exist between

normal vs. low grade pre-cancer (*) for τ_2 and α_2, and between normal vs. high grade pre-cancer (*) for τ_2.

Figure 3: Mean and standard error of the cellular coefficient of variation (cell standard deviation / cell mean) for τ_2 (protein-bound NADH lifetime) and α_2 (percent contribution of protein-bound NADH) for all normal cells (n=81 cells), low grade pre-cancerous cells (n=72 cells) and high grade pre-cancerous cells (n=111 cells) measured in the hamster cheek pouch *in vivo* at 780 nm excitation. The coefficient of variation assesses the extent of variability within a cell relative to its mean (intracellular variability) (32). Unpaired Wilcoxon Rank Sum Tests (and t-tests) revealed statistically significant differences ($p<0.05$) in the coefficient of variation of τ_2 and α_2 between normal cells and all pre-cancerous cells (*), and in the coefficient of variation of α_2 between low grade and high grade pre-cancerous cells (†) ($p<0.05$).

Table 1

(a)

High Density	τ_2 (ns)	α_2 (%)	FAD/(NADH+FAD)
Control (n=8 images)	2.37 ±0.02	30 ± 1	0.60 ± 0.03
3-bromopyruvate (n=6 images)	2.42 ± 0.01*	28 ± 1*	0.70 ± 0.05*
$CoCl_2$ (n=6 images)	2.31 ± 0.03*	28 ± 1*	0.52 ± 0.02*

*Control vs. 3-bromopyruvate / $CoCl_2$ $p<0.05$

(b)

Low Density	τ_2 (ns)	α_2 (%)	FAD/(NADH+FAD)
Control (n=5 images)	2.44 ± 0.02	30 ± 1	0.55 ± 0.02
3-bromopyruvate (n=6 images)	2.52 ± 0.02*	28 ± 1*	0.64 ± 0.02*
$CoCl_2$ (n=6 images)	2.38 ± 0.01*	27 ± 1*	0.52 ± 0.01*

*Control vs. 3-bromopyruvate / $CoCl_2$ $p<0.05$

Figure 1

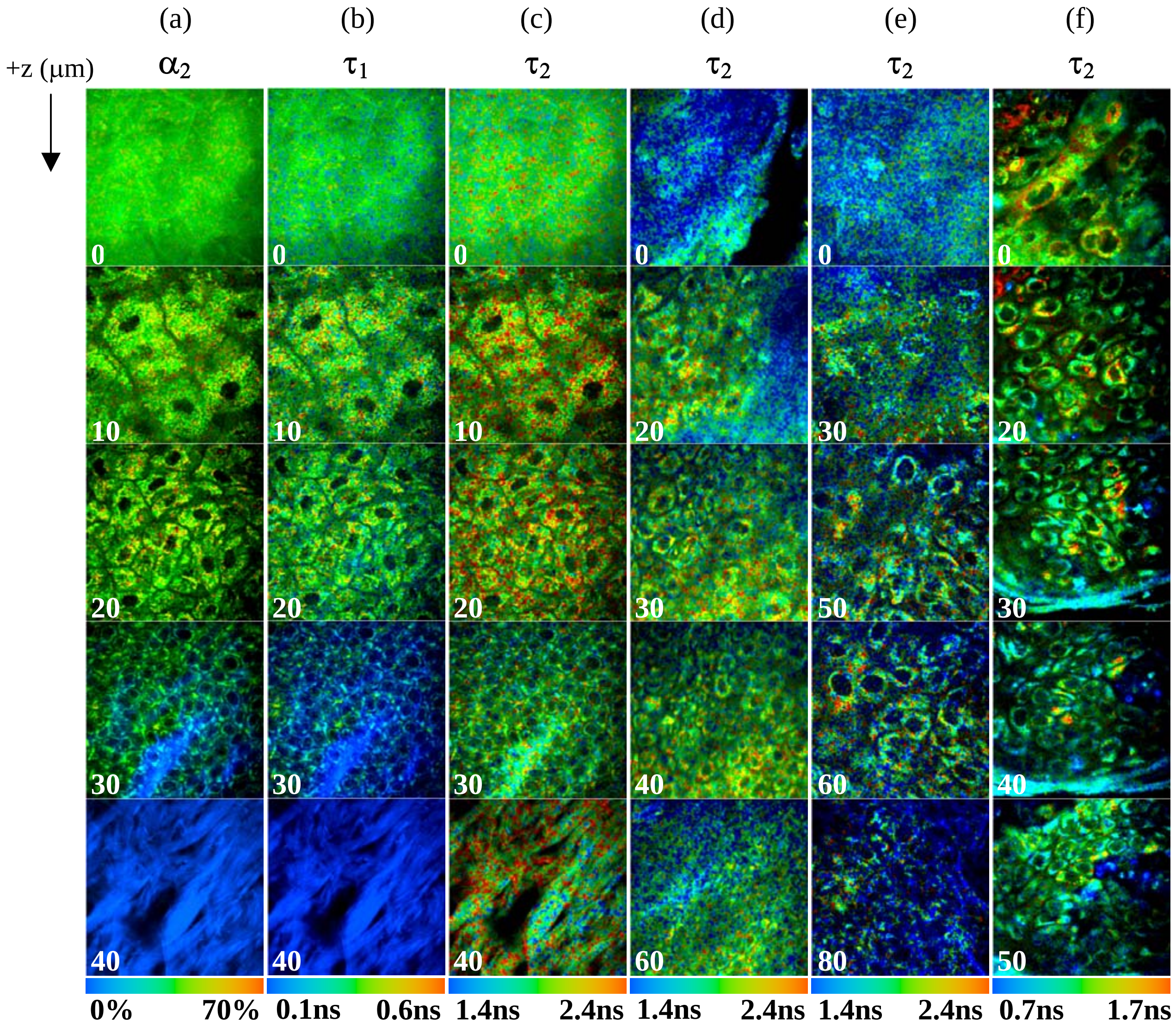
(a)
(b)
(c)
(d)
(e)
(f)
+z (μm)
α_2
τ_1
τ_2
τ_2
τ_2
τ_2
0
0
0
0
0
0
10
10
10
20
30
20
20
20
20
30
50
30
30
30
30
40
60
40
40
40
40
60
80
50
0%
70%
0.1ns
0.6ns
1.4ns
2.4ns
1.4ns
2.4ns
1.4ns
2.4ns
0.7ns
1.7ns

Figure 2

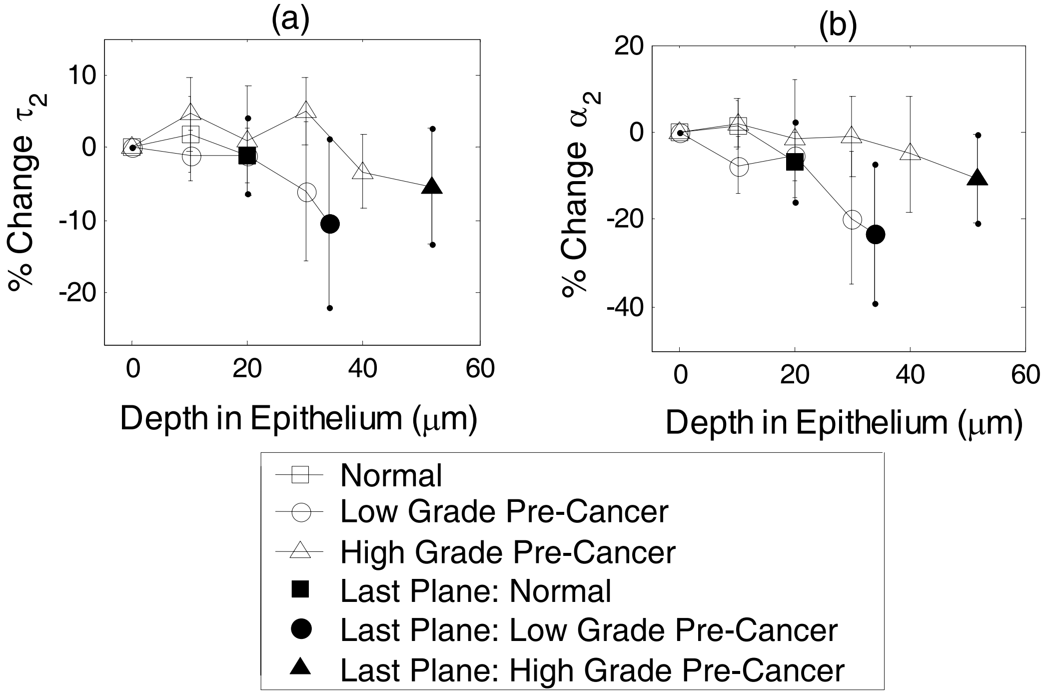
(a)
10
0
-10
-20
% Change τ_2
0
20
40
60
Depth in Epithelium (μm)
(b)
20
0
-20
-40
% Change α_2
0
20
40
60
Depth in Epithelium (μm)
Normal
Low Grade Pre-Cancer
High Grade Pre-Cancer
Last Plane: Normal
Last Plane: Low Grade Pre-Cancer
Last Plane: High Grade Pre-Cancer

Table 2

	τ_2 (ns)	α_2 (%)
Normal (n=9 animals)	2.03 ± 0.06	37 ± 3
Low Grade (n=6 animals)	1.58 ± 0.35*	32 ± 4*
High Grade (n=6 animals)	1.83 ± 0.16*	37 ± 4

* Normal vs. low grade / high grade pre-cancer $p<0.05$

Figure 3

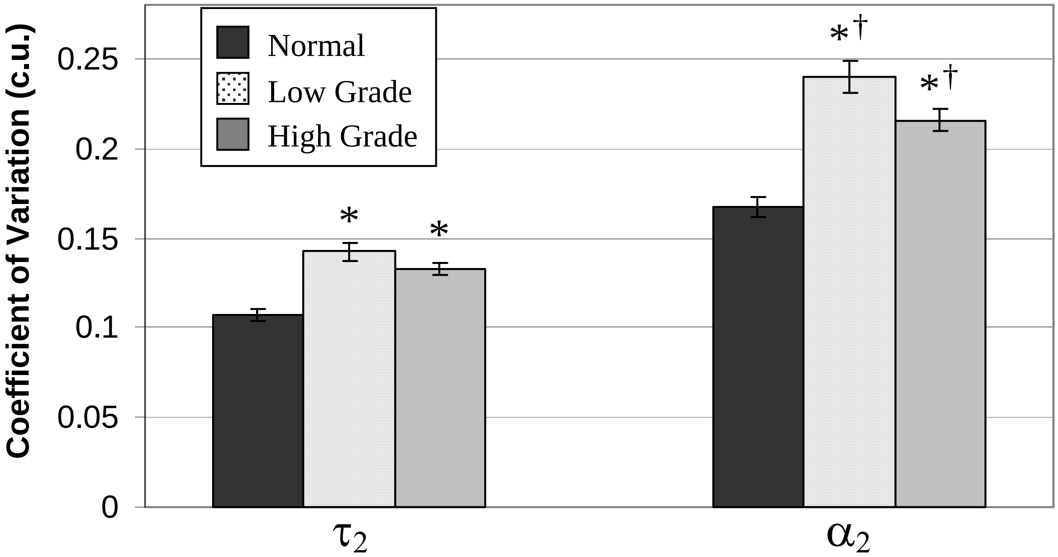

* Normal vs. low grade / high grade pre-cancer $p<0.05$
† Low grade vs. high grade pre-cancer $p<0.05$